# MASS ESTIMATES OF X-RAY CLUSTERS

August E. Evrard<sup>†</sup>

Physics Department, University of Michigan, Ann Arbor, MI 48109-1120 USA evrard@umich.edu

Christopher A. Metzler
NASA/Fermilab Astrophysics Center, Batavia, IL 60510-0500 USA

metzler@umich.edu

and

Julio F. Navarro<sup>†</sup>
Steward Observatory, University of Arizona, Tucson, AZ 85721 USA

inavarro@as.arizona.edu

#### Abstract

We use cosmological gas dynamic simulations to investigate the accuracy of galaxy cluster mass estimates based on X-ray observations. The experiments follow the formation of clusters in different cosmological models and include the effects of gravity, pressure gradients, and hydrodynamical shocks. A subset of our ensemble also allows for feedback of mass and energy from galactic winds into the intracluster medium. We find that mass estimates based on the hydrostatic, isothermal  $\beta$ -model are remarkably accurate when evaluated at radii where the cluster mean density is between 500-2500 times the critical density. Applied to 174 artificial ROSAT images constructed from the simulations, the distribution of the estimated-to-true mass ratio is nearly unbiased and has a standard deviation of 14-29%. The scatter can be considerably reduced (to 8-15%) by using an alternative mass estimator that exploits the tightness of the mass-temperature relation found in the simulations. The improvement over  $\beta$ -model estimates is due to the elimination of the variance contributed by the gas outer slope parameter. We discuss these findings and their implications for recent measurements of cluster baryon fractions.

 $<sup>^{\</sup>dagger}$  also Institute for Theoretical Physics, University of California, Santa Barbara, CA 93106

### 1. Introduction

Estimates of the total masses of groups and clusters of galaxies have been used to infer the amount of dark matter in the universe for over sixty years. A novel technique for estimating the density parameter  $\Omega_0$  makes use of precise measurements of the visible, baryonic mass fraction  $f_b$  in galaxy clusters along with limits on the universal baryon fraction  $\Omega_b$  derived from primordial nucleosynthesis. White *et al.* (1993) showed that cluster baryon fractions, defined as the ratio of the mass in galaxies and intracluster gas to the total cluster mass, should not differ substantially from the universal value,  $\Omega_b/\Omega_0$ , when determined near the outer boundary of their hydrostatic regions — roughly an Abell radius for a cluster as rich as Coma. A straightforward and unbiased estimate of the density parameter is formed by  $\Omega_0 = \Omega_b/f_b$ .

Recent measurements in rich clusters (Briel, Henry & Bohringer 1992; Durret et al. 1994; David, Jones & Forman 1995; White & Fabian 1995) and poor clusters and groups (Ponman et al. 1994; Pildis, Bregman & Evrard 1995; Neumann & Bohringer 1995) indicate  $f_b \geq 0.04 \, h^{-3/2}$ . (Hereafter we write Hubble's constant as  $100 \, h$  km s<sup>-1</sup> Mpc<sup>-1</sup>.) Taken with the nucleosynthesis determination  $\Omega_b \simeq 0.0125 h^{-2}$  (Walker et al. 1991), this implies a rather small value of the density parameter,  $\Omega_0 < 0.3 h^{-1/2}$ , unless primordial nucleosynthesis calculations have underestimated the universal baryon fraction by almost a factor of three. Although there is current debate about the uncertainty in primordial nucleosynthesis determinations of  $\Omega_b$  (Krauss & Kernan 1994; Copi, Schramm & Turner 1995; Hata et al. 1995; Steigman 1995; Sasselov & Goldwirth 1995), current interpretation of the data appear to rule out the large values of  $\Omega_b$  required for consistency with a universe with closure density.

These upper limits on  $\Omega_0$  are especially strong because most of the baryons in clusters are in the hot intracluster medium (ICM), a component empirically found to be more extended than the dark matter distribution (e.g., David et al. 1995). Numerical simulations show that this is a general result of hierarchical scenarios, where clusters are formed through mergers of protoclusters during which energy is transferred systematically to the gas from dark matter (Navarro & White 1993; Pearce, Thomas & Couchman 1994). The results imply that cluster baryon fractions, measured at radii encompassing a density contrast of a few hundred, should be about 10 - 20% lower than the universal value (Evrard 1990; Cen & Ostriker 1992).

Several solutions have been proposed to rescue  $\Omega = 1$  from what has been deemed the cluster "baryon catastrophe" (Carr 1993). A low Hubble constant  $H_0 \lesssim 30 \text{ km s}^{-1} \text{ Mpc}^{-1}$  can alleviate the problem (Bartlett *et al.* 1995), but is in strong disagreement with recent observational estimates which favour a high value for  $H_0$  (Freedman *et al.* 1994; Mould *et al.* 1995). A simple possibility which has not yet been explored in detail is that the binding masses inferred from X–ray observations may be systematically underestimated

by a significant amount. These estimates usually rely on assumptions such as spherical symmetry, hydrostatic equilibrium for the gas, and virial equilibrium for the galaxies, none of which may be fully realized in practice. Clusters exhibit signatures of substructure both in the ICM (Mohr et al. 1995; Buote & Tsai 1995) and in their galaxy distributions (Dressler & Schectman 1988; Bird 1995; Crone, Evrard & Richstone 1995), suggestive of recent mass accretion and of significant departures from equilibrium. A moderate bias in the mass estimates introduced by these effects would have important consequences for the  $\Omega_0$  limits derived by the above arguments.

Discrepancies of  $\sim 50\%$  have, in fact, been reported when mass estimates of the central regions of clusters derived from X-ray observations are compared with those required to produce strong arcs by gravitational lensing of background galaxies (Miralde-Escudé & Babul 1995). Although this discrepancy could signal significant departures from hydrostatic equilibrium or support from non-thermal sources such as magnetic fields (Loeb & Mao 1994), systematic errors in the lensing mass estimates due to projection effects and substructure are more likely to be responsible for the disagreement (Bartelmann, Steinmetz & Weiss 1995; Bartelmann 1995). In fact, at larger radii, weak gravitational lensing has also been used to measure cluster masses (Tyson, Valdes & Wenk 1990; Bonnet, Mellier & Fort 1994; Fahlman  $et\ al.\ 1994$ ) and the small number of clusters with both X-ray and weak lensing mass estimates show no significant discrepancy between the two (Smail  $et\ al.\ 1995$ ; Squires  $et\ al.\ 1995$ ), although the statistical uncertainties are still large.

In this paper, we examine the accuracy of X-ray binding mass estimates using a large number of high resolution simulations designed to follow the non-linear, dynamical evolution of the gravitationally coupled system of dark matter, gas and (in one set of runs) galaxies in a variety of cosmological models. A total of 58 clusters are drawn from three separate projects using two different Lagrangian hydrodynamical codes. The models are used to generate 174 synthetic ROSAT X-ray images and broad beam temperature estimates. Binding masses are then estimated for these systems in a manner analogous to that applied to observational datasets. These models are therefore ideal for understanding possible systematic effects afflicting cluster mass estimates based on X-ray observations. A recent paper by Schindler (1995) addresses the same issue using a sample of six simulations generated with very different techniques. Our results are in excellent agreement, despite the fact that the numerical methods and data analysis procedures used in the two studies differ in a number of details.

After describing briefly the numerical simulations in §2, we begin by examining the validity of the hydrostatic and isothermal assumptions using the three dimensional velocity and temperature profiles of simulated clusters (§3). We then investigate the accuracy of binding masses estimated using the simplest combination of X-ray imaging and broad beam temperatures (§4). In §5 we discuss how the tight correlation between cluster mass and X-ray temperature can be used to determine binding masses with even greater statistical

accuracy. We conclude in §6 with a brief discussion of some implications of these results.

### 2. Numerical Methods

# 2.1 Sample Description

We use 58 N-body/gas dynamics simulations drawn from three different projects and run with two completely independent Lagrangian codes. In all cases we use the Smoothed Particle Hydrodynamics (SPH) technique to follow the evolution of the gas, and either a  $P^3M$  code or a tree-based N-body code to compute the gravitational interaction between particles. All the simulations assume a standard, cold dark matter (CDM) initial fluctuation spectrum with  $\Gamma \equiv \Omega h = 0.5$ . We neglect the radiative cooling of the gas, as well as magnetic fields as a possible source of pressure support. We take the baryon density parameter to be 0.1, and use a Hubble constant of 50 km s<sup>-1</sup> Mpc<sup>-1</sup> (h = 0.5) when scaling to physical units. Details of the models can be found in the references quoted below.

The first set consists of 28 runs from Chris Metzler's thesis (Metzler 1995), which examines the effects of energy feedback and mass ejecta from early type galaxies on the evolution of the intracluster medium (ICM). The set consists of 14 clusters of different mass obtained by constraining the initial density field in cubic, periodic regions ranging from 25 to 60 Mpc (Bertschinger 1987). Each realization is run twice, once including the effects of galaxy feedback and a second, control run without feedback. We shall refer to each of these samples as "EJ" and "2F", respectively. All of the runs assume  $\Omega=1$ . Each simulation uses a total of 65,536 particles, divided equally between gas and dark matter. A description of the feedback implementation and application to the formation of a Coma–sized cluster can be found in Metzler & Evrard (1994). The full set of runs is described in Metzler & Evrard (1995). A salient feature of the ejection runs is that they employ a rather extreme model of galactic feedback, in which early-type galaxies lose half their initial mass by winds. The EJ and 2F series are intended to define an envelope within which realistic models of feedback should lie.

The second set of runs is a sample of 24 used to investigate the X-ray cluster morphology-cosmology connection by Evrard et al. (1993) and Mohr et al. (1995). For this project, eight different realizations of the initial density field were evolved within three background cosmologies in periodic cubes ranging from 30 to 60 Mpc in length. Again, 65, 536 particles per run were used. The cosmological models explored were the standard CDM scenario (model "EdS";  $\sigma_8 = 0.59$ ,  $\Omega = 1$ ), an unbiased, open CDM universe (model "Op2";  $\sigma_8 = 1.0$ ,  $\Omega_0 = 0.2$ ,  $\lambda_o = 0$ ) and an unbiased, low density universe with a flat geometry (model "Fl2";  $\sigma_8 = 1.0$ ,  $\Omega_0 = 0.2$ ,  $\lambda_o = 0.8$ ). Here  $\sigma_8$  is the rms mass fluctuation in spheres of  $8h^{-1}$  Mpc, and  $\Omega_0$  and  $\lambda_0$  are the present values of the density parameter and the cosmological constant, respectively. An important aspect of this set is that the runs corresponding to each cosmology share common dynamical histories through the use of the same eight

initial density fields. The benefit of this procedure is that relative differences between the final characteristics of clusters can be ascribed to the effect of the different cosmological backgrounds rather than to "cosmic scatter" in the initial density fields.

The final set consists of six models taken from Navarro, Frenk & White (1995a; model "NFW") which were used to examine the evolution of scaling laws relating the dynamical and X-ray properties of clusters of different mass. These simulations were evolved with a code completely independent from the one used in the runs described above; a Tree/SPH code described in detail in Navarro & White (1993, 1994). The six clusters were identified at z = 0 ( $\sigma_8 = 0.63$ ) in the cosmological N-body simulations of Frenk et al. (1990), and then resimulated individually at higher resolution. Each simulation has 21, 296 particles, half gas and half dark matter, distributed over boxes of size 15-50 Mpc, depending on the mass of the cluster. The tidal field due to material surrounding each cluster out to 360 Mpc is treated self-consistently by coarse sampling the surrounding matter with particles of radially increasing mass.

The ensemble of simulations span a wide range in mass and temperature, from  $\sim 10^{14}$  to  $3\times 10^{15}M_{\odot}$ , and from  $\sim 1$  to 10 keV. Table 1 provides a summary for future reference of the runs and the notation that we use. The clusters produced in the different projects have similar spatial and mass resolution properties. The ratio between the size of a simulated cluster (as measured by the radius,  $r_{500}$ , where the mean density relative to the critical value is 500) and the gravitational softening is in the range  $10 \lesssim r_{500}/\varepsilon \lesssim 30$ . The runs have similar numbers of particles within  $r_{500}$ , typically 5000 in each component.

### 2.2 Hydrostatic, Isothermal Mass Estimates

The typically smooth morphology of the X-ray emission from the hot, intracluster medium leads naturally to the hypothesis that the gas is near equilibrium, stratified along isopotential surfaces in a mildly evolving distribution of dark matter, gas and galaxies. The assumption of hydrostatic equilibrium — the balance between pressure gradients and gravity — for gas supported solely by thermal pressure, results in a direct measure of the binding mass M(r). Assuming spherical symmetry,

$$M(r) = -\frac{kT(r)}{G\mu m_p} r \left( \frac{\mathrm{d}\log \rho(r)}{\mathrm{d}\log r} + \frac{\mathrm{d}\log T(r)}{\mathrm{d}\log r} \right) \tag{1}$$

where  $\rho(r)$  and T(r) are the gas density and temperature profiles, k is Boltzmann's constant, and  $\mu m_p$  is the mean molecular weight of the gas. In principle, all terms on the right hand side of this equation are measurable. The main limitation is that one must deconvolve three dimensional profiles from two dimensional surface brightness information. This requires knowledge of, or a model for, the temperature profile T(r). Since direct measurements of the temperature as a function of radius T(r) (more precisely, the X-ray emission-weighted projected temperature) are still a relatively rare commodity, the

common practice has been to assume that the gas is isothermal at the spatially averaged temperature  $T_{\rm X}$  determined from a broad beam spectroscopic instrument such as EXOSAT or Ginga. Preliminary ASCA results (Ikebe et~al.~1994; Mushotzky 1994), as well as previous direct measurements (see, e.g., Watt et~al.~1992) and the numerical models that we use here generally support this assumption (see §3.3 below).

The usual parametrization of the density profile of the ICM is based on the isothermal,  $\beta$ -model proposed by Cavaliere & Fusco-Femiano (1976),  $\rho_{\rm ICM}(r) = \rho_o (1 + (r/r_c)^2)^{-3\beta/2}$ . With this assumption, equation (1) reduces to

$$M(r) = \frac{3\beta}{G} \frac{kT_{\rm X}r}{\mu m_p} \frac{(r/r_c)^2}{1 + (r/r_c)^2} = 1.13 \times 10^{15} \beta \frac{T_{\rm X}}{10 \text{ keV}} \frac{r}{\text{Mpc}} \frac{(r/r_c)^2}{1 + (r/r_c)^2} \,\mathrm{M}_{\odot}, \qquad (2)$$

assuming  $\mu = 0.59$  for the second equality. For an isothermal gas, the X-ray surface brightness as a function of projected radius  $S_X(\theta)$  simply reflects the integrated emission measure and can be expressed as

$$S_X(\theta) = S_0 (1 + (\theta/\theta_c)^2)^{-3\beta + 1/2}.$$
 (3)

X-ray spectroscopy provides  $T_X$ , while estimates of  $\beta$  and  $r_c$  are obtained from X-ray imaging.

To mimic the mass estimates derived from X-ray observations, we generate for each simulated cluster three artificial ROSAT images and emission weighted temperatures  $T_{\rm X}$  along the principal axes of the volume. Generating synthetic ROSAT images requires a choice of several parameters, including: (i) the cluster redshift z, (ii) the exposure time  $t_{exp}$ , and (iii) the background noise level  $S_N$ . Fitting the resulting surface brightness profiles to the  $\beta$ -model introduces two additional parameters; (iv) the background subtraction level  $S_b$  and (v) the minimum flux level to which the fit is performed  $S_{min}$ . An additional choice is the energy band of the observations, which we take to be the full ROSAT band 0.1-2.4 keV. Because there is no obscuring galaxy in our 'observations', our results are insensitive to the exact choice of the lower energy limit for the band employed. We use emission weighted temperatures within circular apertures large enough to contain nearly all the cluster emission. Since most of the photons come from the central regions of the cluster, the estimates of  $T_{\rm X}$  are rather insensitive to the aperture choice.

We use a single parameter set to construct the synthetic images of all model clusters, chosen to be representative of typical X-ray observations. We view the clusters at a redshift z = 0.04, image them for  $t_{exp} = 7200$  s, include a Poisson background in the counts at a level of  $3 \times 10^{-4}$  cnts s<sup>-1</sup> arcmin<sup>-2</sup>, subtract a mean background with exactly this value, and fit each to the  $\beta$ -model out to the radius at which the corrected counts reach the background level. We use emission weighted temperatures in the same ROSAT band, measured within an angular scale of 16', corresponding to a fixed metric radius of

1.04 Mpc. These parameter values are summarized in Table 2. We investigated alternative parameter sets, and found that the results depended mainly on the image quality through the combination of redshift, exposure time and assumed background. The parameter choices above provide high signal-to-noise images for the majority of the sample.

For each cluster, the three images and emission weighted temperature maps are generated and reduced to obtain the values of  $\beta$ ,  $r_c$  and  $T_{\rm X}$ . This procedure works very well for clusters formed in cosmological models with  $\Omega=1$ . However, as discussed in Mohr *et al.* (1995), in low density universes the emission profiles of the cluster models are strongly peaked, resulting in unacceptably poor  $\beta$ -model fits. In this case, we decided to excise the central regions and to fit only data outside a region of angular radius 4', corresponding to a linear scale of 260 kpc (see Mohr *et al.* 1995 for details). Typical statistical uncertainties in the fitted parameters are  $\lesssim 5\%$ , but in a few cases the uncertainties can be as high as  $\sim 40\%$ . Once  $\beta$ ,  $r_c$  and  $T_{\rm X}$  have been determined, we can estimate the binding mass as a function of radius using equation (2).

# 2.3 A Particular Example

Before examining results for the entire sample, we discuss data for a particular cluster which highlight characteristics typical of the ensemble. Figure 1 shows X-ray surface brightness and emission weighted temperature maps, as well as the emission weighted projected velocity field for the ICM in a cluster taken from the EdS sample. The field of view in each of the panels is 64', corresponding to 4.2 Mpc at the assumed cluster redshift of 0.04. Two of the three projections show a bimodal central structure; the result of a recent merger involving two main sublumps with mass ratio 2.8:1. Infall patterns of the sublumps are evident in the velocity field of the middle (y-axis) projection. The temperature map shows significant variations (up to a factor  $\sim$ 2) in temperature on scales of a few hundred kpc. The hot spots occur in regions where the gas is being compressed and mildly shocked by the interpenetrating subcluster cores. Cooler gas can be seen trailing in the wake of the substructure cores.

Several of the features of this simulated cluster, particularly the y-axis view, are reminiscent of the cluster A2256. Features in common include a bimodal central structure and spatial variations in temperature similar in morphology and amplitude (Briel et al. 1991; Miyaji et al. 1993; Briel & Henry 1994). Furthermore, an offset, extended radio halo exists in A2256 which strongly indicates the presence of a flow pattern similar to that seen in the y-axis image (Rottgering et al. 1994).

Figure 2 shows the azimuthally averaged X-ray surface brightness and emission weighted temperature profiles for the three projections. Surface brightness profiles are scaled down successively by an order of magnitude for the sake of clarity; as are the temperature profiles by factors of 2. Values of the fitted parameters are  $r_c = 294 \pm 6$ ,  $384 \pm 10$ , and  $359 \pm 9$  kpc; and  $\beta = 0.89 \pm 0.02$ ,  $0.85 \pm 0.02$ , and  $0.81 \pm 0.02$  for the three projections from top to

bottom, respectively.

Although significant spatial variations in temperature are obvious in Figure 1, the radially averaged temperature profile is close to isothermal over a significant fraction of the cluster image. The temperature varies by  $\lesssim 20\%$  within 10′, a region wherein the surface brightness drops by a factor of 30. The temperature drops by a factor of 2 at about 20′ from the center, but the surface brightness at this radius is already below the adopted background of  $3 \times 10^{-4}$  cnts s<sup>-1</sup> arcmin<sup>-2</sup>.

From Figure 1 we learn the importance of examining spatial temperature maps directly, since a flat azimuthally averaged profile need not be indicative of a truly isothermal ICM. Comparison of the temperature and surface brightness maps can provide useful dynamical clues, although geometry plays an obscuring role. From the single dynamical configuration corresponding to the cluster in Figure 1 one can get, depending on projection (from top to bottom), (i) a fairly relaxed X-ray image with asymmetric temperature map and strong velocity gradients; (ii) a bimodal X-ray image with an "S"-shaped hot spot resulting from a symmetric infall pattern and (iii) a bimodal X-ray image with a peanut-shaped hot spot and a relatively modest velocity field in projection.

# 3. Is the ICM Hydrostatic and Isothermal?

The assumption of hydrostatic equilibrium underlies the X-ray mass estimate method, and the assumption of isothermality greatly simplifies it. In this section, we analyze how close to hydrostatic equilibrium and isothermality the cluster models are by inspecting directly their three dimensional velocity and temperature fields.

# 3.1 The ICM Velocity Field

Figure 3 shows the radial Mach numbers  $\langle v_r \rangle/c_s$  and  $\langle v_r^2 \rangle/c_s^2$  derived from the gas sound speed  $c_s^2(r) = 5kT(r)/3\mu m_p$  and the first and second moments of the radial velocity field, respectively. To facilitate comparison between clusters of different sizes, the mean interior density contrast  $\delta_c(r) = 3M(r)/4\pi\rho_c r^3$  is used as the radial variable in the figure, reversed to reflect the correspondence with cluster radius. Note that the density contrast used here is defined with respect to the critical value for closure  $\rho_c = 3~{\rm H_0}^2/8\pi G$  in all the models. The center of the cluster is defined as the position of the most bound dark matter particle, and velocities are calculated with respect to the mean velocity of all cluster particles linked by a standard friends—of–friends algorithm using a linking parameter 0.15 times the mean interparticle spacing. The  $\Omega=1$  runs all exhibit a common structure, with the exception of two of the NFW runs and one EdS run, which are undergoing strong mergers at z=0. The Mach numbers of these systems are significantly higher than the average. The low  $\Omega$  runs have generally quieter velocity fields, as expected given their earlier formation times and, consequently, their dynamical maturity relative to clusters formed in a high density

universe.

The mean radial Mach number  $\langle v_r \rangle/c_s$  has the characteristic signatures expected from gravitational infall (Gunn & Gott 1972). An outer zone of mildly supersonic infall surrounds the 'virial' region of the cluster, within which the gas has been largely thermalized and is close to hydrostatic equilibrium. The infall regime is largely absent in the low  $\Omega$  models, due to the stagnated growth of linear perturbations on large scales. This, however, does not imply that there are no recent merger events in the open universe sample — at least one Op2 cluster is experiencing an ongoing merger event at the present time.

The right-hand panels of Figure 3 provide an upper limit on the ratio of kinetic to thermal pressures for the gas. This ratio rises monotonically with radius, from values < 10% for radii where  $\delta_c > 500$  to values  $\gtrsim 50\%$  at radii where  $\delta_c \lesssim 100$ . A few ongoing mergers are clearly recognized by the large values of the  $\langle v_r^2 \rangle/c_s^2$  ratio near the center. In this case, interpreting the ratio between kinetic and thermal energy as the relative contribution of kinetic and thermal pressures to support the gas does not apply, since the systems are far from equilibrium. As the velocity field in Figure 1 indicates, non-zero values of  $\langle v_r^2 \rangle$  arise during mergers from large-scale bulk motions of the gas across the face of a given radial shell rather than from a local, uniform dispersion on the shell.

From Figure 3, we derive a value  $\delta_c = 500$  as a conservative estimate of the boundary between the inner, virialized region of the clusters and their recently accreted, still settling outer envelopes. Define  $r_{\delta_c}$  as the radius within which the mean interior density is  $\delta_c$  times the critical value. Then, within  $r_{500}$ , the hydrostatic equilibrium assumption is valid since the gas is, on average, neither expanding nor contracting. This estimate is conservative in the sense that, in many clusters, hydrostatic balance appears to hold even at somewhat larger radii. The turnaround radius can be seen to occur at radii about a factor 3-4 larger than  $r_{500}$  (for  $\Omega=1$ ). This is consistent with the spherical infall models of Bertschinger (1985) in which infalling gas is shocked nearly to rest at a radius about a third of the turnaround radius. Despite this nice agreement, we stress that the accretion in these three dimensional models is far from spherically symmetric.

Table 3 gives mass averaged values of the two radial Mach numbers measured within  $r_{500}$  for each set of runs. The mean radial Mach numbers are all quite small, typically a few percent or less, and are consistent with zero given the measured error in the mean. Again, the NFW set seems to be the most dynamically active, as can be seen from the measures of both velocity moments. Typical values of  $\langle v_r^2 \rangle/c_s^2$  are  $\lesssim 10\%$ , indicating that the gas is hydrostatically supported by thermal pressure to this accuracy within  $r_{500}$ .

# 3.2 Cluster Scaling

As discussed above, we will use the radius  $r_{500}$  as a characteristic length scale separating the nearly hydrostatic central region of a cluster from the surrounding, recently accreted outer envelope. As shown by Navarro *et al.* (1995a,b) and Metzler & Evrard (1995), clusters of different mass have similar structures when scaled to such a characteristic radius. This similarity, along with the equilibrium assumption validated above, implies a power–law relationship between cluster 'size' and temperature

$$T \propto \frac{M(\langle r_{500})}{r_{500}} \propto r_{500}^2,$$
 (4)

as appropriate for systems of similar density in virial equilibrium. Figure 4 shows this relationship for the simulations, using the measured value of  $r_{500}$  and three orthogonal measures of the emission weighted temperature  $T_{\rm X}$ . Each cluster appears three times in this plot; the dispersion in  $T_{\rm X}$  for different projections is typically quite small. Fitting the results with a power law, we find

$$r_{500}(T_{\rm X}) = 2.48 \pm 0.17 \left(\frac{T_{\rm X}}{10 \text{ keV}}\right)^{1/2} \text{Mpc}$$
 (5)

where the quoted uncertainty in the intercept is given by the standard deviation of the residuals in the log space fit. The actual best fit slope for each individual set of runs differs by less than 10% from the 0.5 exponent expected from equation (4). There are small offsets between the models. The ejection models, for example, have  $\sim 6\%$  smaller  $r_{500}$  at a given temperature or, equivalently,  $\sim 12\%$  higher emission weighted temperatures for a given  $r_{500}$ , compared to the 2F runs. The slope for the EJ sample is also slightly ( $\sim 10\%$ ) steeper than those of the non-ejection samples, as expected from the differential effect of feedback, which raises the temperature of poor cluster gas proportionally more than that of rich clusters (Metzler & Evrard 1995). There is no significant difference between the NFW, 2F and EdS data sets, indicating an encouraging agreement between the results of models run with completely independent codes for the same cosmological model.

# 3.3 Temperature Profiles

Figure 5 shows the mass-weighted gas temperature, in units of  $T_{\rm X}$ , as a function of the normalized radius  $r/r_{500}$  for all runs. For  $\Omega=1$ , the profiles are close to isothermal within  $r_{500}/2$ , and decline gently beyond that radius; the temperature at  $r_{500}$  is  $\sim 20\%$  lower than at the center. In all cases, the modest drop in temperature within  $r_{500}$  is due to the fact that the density profiles of both gas and dark matter are slightly steeper than isothermal in their outer parts (Navarro *et al.* 1995a,b). In the case of an open universe, the profiles are noticeably steeper; the temperature at  $r_{500}$  is on average a factor of two lower than the central value. This comes as no surprise, for the density profiles of clusters formed

in low-density universes are expected to be significantly steeper than those formed in an  $\Omega=1$  cosmology (Hoffman 1988, Crone, Evrard & Richstone 1994). Since X-ray data rarely extend significantly beyond  $r_{500}$ , an isothermal assumption should be appropriate for most observed clusters.

### 4. Mass Estimates from the $\beta$ -model.

After constructing the synthetic ROSAT images as described in §2.2, fitting the surface brightness with equation (3), and measuring the projected X-ray emission weighted temperature, we derive estimates of the cluster binding mass as a function of radius via equation (2). Once again, in order to compare clusters of different mass (and size), we transform the radial variable into an *estimated* density contrast  $\delta_c^{est}$  relative to the critical density using the estimated mass  $M^{est}(r)$  from eq.(2);

$$\delta_c^{est}(r) \equiv \frac{3M^{est}(r)}{4\pi\rho_c r^3} = \frac{2GM^{est}(r)}{H_0^2 r^3} = \left(\frac{2\sigma(r)}{H_0 r}\right)^2 \tag{6}$$

where  $\sigma^2(r) = GM^{est}(r)/2 r$  is roughly the one-dimensional velocity dispersion of the cluster. For a rich cluster with  $\sigma = 1000 \text{ km s}^{-1}$  at  $r = 1 h^{-1} \text{ Mpc}$ , the estimated density contrast is  $\delta_c^{est} = 400$ . Note that  $\delta_c^{est}$  depends on the combination  $H_0r$ , and therefore it is independent of the Hubble constant, making it a useful measure of radius for observations.

Figure 6 shows the ratio between estimated and true mass as a function of the radial coordinate  $\delta_c^{est}$ . The finite dynamic range in the simulations limits the density contrast to values  $\lesssim 5000$ . This figure shows that the cluster binding masses are on average quite accurately determined at overdensities between 500 and 2500. In the outer regions, where  $\delta_c^{est} \lesssim 200$ , masses are typically overestimated because the estimated mass, assumed to increase linearly with radius, increases with radius faster than the true mass in this region. The effect is more pronounced in the low density runs, where the cluster density profiles are steepest. Overestimates by factors up to 3 are seen in the low-density runs at  $\delta_c^{est} = 100$ .

Figure 7 presents histograms of the estimated-to-true mass ratio at radii corresponding to  $\delta_c^{est} = 2500$ , 500 and 100. These three values of the density contrast sample dynamically different regions and span a range comparable to that of current X-ray observations. Dashed vertical lines in the figure show  $\pm 40\%$  error for reference. The trend toward overestimates at low density contrasts noted in Figure 6 is apparent in the rightmost column. The omission of the NFW runs at this contrast is technical in origin; these simulations do not extend reliably to these low overdensities.

Relatively large (factor  $\sim 2$ ) underestimates occur in a few of the  $\Omega=1$  clusters. Three of the worst offenders arise from images of a single, strongly bimodal EdS cluster which is currently experiencing a major merger. Indeed, ongoing mergers are responsible for six of the worst underestimates at  $\delta_c^{est}=500$ . Synthetic ROSAT images of these cases

are shown in Figure 8. Bold and light circles indicate the estimated and true values of  $r_{500}$ . The complex, multi-peaked structure of the X-ray emission in these images is a strong signal of dynamical unrest. Although such objects would probably be rejected by observers attempting to apply an equation based on hydrostatic equilibrium, we include these cases in our analysis below since they only represent a small fraction of the total population.

The similarity between the  $\Omega=1$  sets suggests that co-adding the runs is appropriate in order to compute the ensemble statistics. Figure 9 shows the histogram of estimated-to-true mass ratios,  $\mathcal{X} \equiv M^{est}/M^{true}$ , evaluated at  $\delta_c^{est}=500$  for the 126 images of the combined EJ, 2F, NFW and EdS sets. The histogram is nearly Gaussian with mean  $\bar{\mathcal{X}}=1.02$  and standard deviation  $\sigma_{\mathcal{X}}=0.29$ . At this density contrast, the  $\beta$ -model estimates are unbiased and have rather modest scatter. We repeated this procedure at contrasts  $\delta_c^{est}=2500$ , 1000, 250 and 100. The means and standard deviations of the resulting estimated-to-true mass ratio distributions are given in Table 4 for the  $\Omega=1$  and  $\Omega_0=0.2$  ensembles. Values in this Table reflect the trends apparent in Figures 6 and 7; the bias and the variance in the mass estimator both increase with increasing radius (i.e., towards lower density contrasts). The increase in the variance with radius is probably linked to the longer dynamical times of the outer regions.

Although the estimator does worse in the case of strongly bimodal clusters (see Figure 8), there are cases where the geometry of the projection, together with the interplay between the estimated values of  $\beta$ ,  $r_c$ , and  $T_{\rm X}$ , can result in accurate mass estimates even for clusters with suspicious looking X-ray images. As an example, consider the cluster shown in Figure 1. The  $\delta_c^{est}=500$  mass estimates for the three orthogonal projections yield (from top to bottom)  $\mathcal{X}=1.17$ , 1.02 and 0.97. The most symmetric X-ray image incurs the largest error while the two images displaying core bimodality are more accurately determined. Note that  $r_{500}$  for this cluster is 1.62 Mpc, or 24' in the figure, well beyond the core region. The larger value in the top projection compared to the others is due to slightly larger values of  $\beta$  and  $T_{\rm X}$  and a smaller core radius compared to the other projections. These values result from the fact that the line of sight in the top panel is nearly parallel to the collision axis of the penetrating cores.

In summary, we find  $\beta$ -model mass estimates to be nearly unbiased and accurate to a few tens of percent in the regime  $250 \lesssim \delta_c^{est} \lesssim 2500$  for the  $\Omega = 1$  models and  $\delta_c^{est} \gtrsim 1000$  for the  $\Omega_0 = 0.2$  sample. A bias toward overestimating masses exists at low values of  $\delta_c^{est}$ . Clusters with strongly bimodal or more complex images involve the largest mass underestimates. Because of the interplay of  $T_x$ ,  $\beta$  and  $r_c$ , there is not a simple, general connection between the properties of the X-ray image and the accuracy of the mass estimates obtained with the  $\beta$ -model.

# 5. Estimates Based on Cluster Scaling Relations.

As discussed in §3.2, massive clusters within a given cosmology exhibit a remarkably similar structure when scaled to a fixed density contrast. Together with the condition of virial or hydrostatic equilibrium, this implies that the temperature of a cluster is, on its own, a good indicator of the size and mass of the system. Figure 4 shows this result very clearly. The tight correlation shown in this figure between  $T_{\rm X}$  and  $r_{500}$  implies a similarly tight correlation between mass and temperature since, by definition, the mean density within  $r_{500}$  is 500 times the critical density. Armed only with the broad beam temperature measure  $T_{\rm X}$ , we can thus form an estimate

$$M_{500}^{est}(T_{\rm X}) \equiv 500 \frac{4\pi}{3} \rho_c(r_{500})^3 = 2.22 \times 10^{15} \left(\frac{T_{\rm X}}{10 \,\text{keV}}\right)^{3/2} M_{\odot}$$
 (7)

for the mass within the radius  $r_{500}(T_X)$  given by equation (5).

We compare this mass estimate with the true mass within  $r_{500}(T_{\rm X})$  for the  $\Omega=1$  ensemble in Figure 10. (Results for the  $\Omega_0=0.2$  sets are similar.) The distribution of estimated-to-true mass ratios is nearly Gaussian with a standard deviation of only 15%. Note that, in this case, no cluster in the  $\Omega=1$  sets has its mass over or underestimated by more than 40%, regardless of its dynamical state. This procedure can be extended to other values of the density contrast in a straightforward way. For a given  $\delta_c$ , we compute the characteristic radii  $r_{\delta_c}$  from the numerical sample and fit them to a relation of the form

$$r_{\delta_c}(T_{\rm X}) = r_{10}(\delta_c) \left(\frac{T_{\rm X}}{10 \text{ keV}}\right)^{1/2} \tag{8}$$

where the normalization  $r_{10}(\delta_c)$  is the average radial scale of 10 keV clusters at density contrast  $\delta_c$ .

The resulting distributions of  $\mathcal{X}$  are unbiased by construction and have standard deviation  $\sigma_{\mathcal{X}}$ . Table 5 shows the characteristic radii  $r_{10}(\delta_c)$  and the scatter in the mass estimator  $\sigma_{\mathcal{X}}$  for density contrasts  $\delta_c = 100$ , 250, 500, 1000 and 2500. Slight offsets in the characteristic radii are evident between the high and low  $\Omega$  cosmologies, consistent with the difference in cluster density profiles. As in the  $\beta$ -model estimates, the scatter in the mass estimates increases with radius. At density contrasts of a few thousand, the uncertainty in the mass estimates is extremely small  $\sigma_{\mathcal{X}} \lesssim 10\%$ .

Another way to interpret these results is to consider that the scaling law mass estimate is consistent with the hydrostatic,  $\beta$ -model estimate, equation (2), when evaluated at  $r_{500}(T_{\rm X})$  with a characteristic value of  $\beta$  given by

$$\beta_* = 0.79 (1 + (r_c/r)^2). (9)$$

The second term is a typically small ( $\lesssim 5\%$ ) correction at  $\delta_c = 500$ . This value for  $\beta$  compares well with measured values of  $\beta$  for many well studied, rich X–ray clusters, among them Coma (Hughes 1989) and A2256 (Briel *et al.* 1992).

Why are the scaling law estimates more accurate than those of the  $\beta$ -model? Consider the variance in the  $\beta$ -model mass estimated at a fixed radius

$$\left(\frac{\Delta M}{M}\right)^2 = \left(\frac{\Delta T_{\rm X}}{T_{\rm X}}\right)^2 + \left(\frac{\Delta \beta}{\beta}\right)^2 + 2\left(\frac{\Delta T_{\rm X}}{T_{\rm X}}\frac{\Delta \beta}{\beta}\right).$$
(10)

In a universe filled with perfectly hydrostatic, self-similar clusters, all clusters would follow a  $r_{\delta_c}(T_{\rm X})$  relation like equation (8) exactly and all would have a fixed value  $\beta_*$  for their outer profile slope. Introduction of perturbations in temperature and density off this perfect sequence will lead to a non–zero variance in the mass estimate. The only way to retain perfect mass estimates is to introduce correlated perturbations  $\Delta \beta/\beta \equiv -\Delta T_{\rm X}/T_{\rm X}$  in density and temperature, so that hydrostatic equilibrium is maintained. Uncorrelated perturbations in  $\beta$  and  $T_{\rm X}$  will lead to a larger variance than that arising from perturbations in one parameter alone.

Figure 11 shows the perturbations measured directly in the simulations. Perturbations in  $\beta$  are defined with respect to the average,  $\beta_* = 0.79$ , while those in temperature are defined with respect to the mean radius–temperature relation, using the known value of  $r_{500}$  to define the unperturbed cluster temperature for each cluster. It is clear from this Figure that the data exhibit no correlation between  $\Delta\beta/\beta$  and  $\Delta T_{\rm X}/T_{\rm X}$ . The larger variance in the  $\beta$ -model compared to the scaling law mass estimates can thus be understood as arising from an additional, independent source of error in the  $\beta$ -model estimator; the introduction of  $\beta$  from X-ray imaging is essentially adding noise to the mass estimates. As a concrete example, consider again the three images in Figure 1. The  $\beta$ -model mass estimates yield  $\mathcal{X} = 1.17$ , 1.02 and 0.97 from top to bottom whereas the scaling law results are  $\mathcal{X} = 1.05$ , 1.00 and 0.99, respectively.

The "noise" added by the measured values of  $\beta$  has several sources. Recent dynamics play a role. Clusters are not in exact hydrostatic balance, particularly in their outer parts. The present density and temperature structure can be perturbed by prior mergers and accretion. Geometry also plays a role. The cluster gas distribution is, in general, ellipsoidal rather than spherical and the measured values of  $\beta$  are obtained from projected, two-dimensional images of the three-dimensional density distribution. Finally, values of  $\beta$  derived from surface brightness fits are sensitive to contamination from foreground/background sources, choice of cluster center, as well as image quality and technical aspects of data reduction procedures. These concerns are compounded when one considers the basic fact that  $\beta$  is a measure of the derivative of the logarithm of the surface brightness.

The scaling law method is superior to the  $\beta$ -model because of its smaller variance. Its accuracy is also remarkably insensitive to the dynamical state of clusters and the cosmo-

logical background. Its main drawback is the reliance on numerical experiments to provide the normalization,  $r_{10}(\delta_c)$ , of equation (8) which, in turn, depends on the particular structure formation model under scrutiny, and may depend as well on the numerical method used in the investigation. Regarding the latter, we are encouraged by the good agreement shown between two independent codes used in this study. We anticipate future studies by groups employing independent numerical methods will address the robustness of the normalization  $r_{10}(\delta_c)$ . We also find room for optimism in the rather modest sensitivity to  $\Omega_0$  displayed by the normalization and scatter in mass estimates shown in Table 5. This insensitivity may be rooted in the fact that the scaling laws merely reflect the condition of virial equilibrium within  $\delta_c \sim \mathcal{O}(10^3)$ . Overall, these results show that it is possible to use X-ray spectroscopy to estimate cluster masses with an rms accuracy substantially better than 20%.

### 6. Discussion and Conclusions.

The results described in the previous sections agree well with those of Schindler (1995), who found biases and variance of a few tens of percent or less in the "normal cluster" sample derived from the numerical simulations of Schindler & Böhringer (1993) and Schindler & Müller (1993). The simulations and analysis methods in those works differ in many respects from those used here. In particular, the Eulerian gas dynamics scheme adopted in their study captures shocks more accurately than the SPH technique used here, while the adaptive nature of the SPH smoothing kernel provides better spatial and mass resolution in high density regions. Given the significant differences between the independent simulation algorithms used in these studies, we find the degree of qualitative and quantitative agreement rather encouraging.

Tsai, Katz & Bertschinger (1994) also examined the accuracy of the  $\beta$ -model mass estimates applied to an SPH simulation which included radiative cooling for the gas, but which excluded the effects of galaxy formation and feedback. At 1 Mpc from their cluster center, where  $\delta_c \simeq 700$ , they found that the  $\beta$ -model overestimated the mass by  $\sim 25\%$ , typical of the uncertainties found in our analysis. They also found large underestimates at radii near the core radii of their surface brightness fits ( $\sim 200 \text{ kpc}$ ) which arose, in part, from the presence of a strong gradient in the gas temperature near the center. However, at these high density contrasts, their results are compromised by the artificially strong concentration of baryonic material near the center.

The improved variance of the scaling law estimates over the  $\beta$ -model is a mixed blessing. A serious concern is the sensitivity of the slope and normalization of the  $r_{\delta_c} - T_{\rm X}$  relation to the assumed cluster physics and the underlying cosmological model. We find very modest sensitivity to  $\Omega_0$  near  $\delta_c \simeq 10^3$  (Table 5) and find that the ejection models do not differ substantially from the infall sample. We suspect, and this suspicion is supported by collisionless simulations of cluster formation (Crone *et al.* 1994), that the impact of

changing the initial perturbation spectrum will be less than that of varying  $\Omega_0$ , but this issue remains to be investigated in detail.

What should then an observer with X-ray data do to estimate a cluster's mass? It depends on whether it is more important to minimize the bias or the variance in the mass estimate. For example, when comparing a set of X-ray derived masses to values derived using an independent method (e.g., weak gravitational lensing), minimizing the bias in the X-ray binding masses would perhaps be most important, and the  $\beta$ -model approach preferred. On the other hand, if one were looking for the slope of correlations between an observable cluster property (e.g., optical luminosity or velocity dispersion) and binding mass, then minimizing the variance would be more important, and the scaling law method preferred.

To summarize, we have used an ensemble of 58 gas dynamics cluster simulations to investigate the accuracy of binding mass estimates based on the hydrostatic, isothermal  $\beta$ -model and on the temperature–mass relation. We have also analysed the velocity and temperature fields of the numerical models to address the questions of hydrostatic equilibrium and isothermality. A summary of our main results follows.

- Within a radius,  $r_{500}$ , where the cluster mean interior density is  $500\rho_c$ , the gas velocity field is extremely quiet (Table 3 and Figure 3), validating the basic assumption of hydrostatic support by thermal pressure. Despite local variations in temperature due to ongoing merger events (Figure 1), the radially averaged gas temperature is nearly isothermal within  $r_{500}$  in the  $\Omega = 1$  sample. The  $\Omega_0 = 0.2$  clusters exhibit a moderate, negative radial temperature gradient.
- The standard  $\beta$ -model mass estimator (eq. 4) is nearly unbiased and has a modest scatter in regions where the mean estimated density contrast is in the range  $500 \lesssim \delta_c^{est} \lesssim 2500$ . For example, at  $\delta_c^{est} = 1000$ , the mean value of  $M^{est}/M^{true}$  is 0.94 (1.15) with standard deviation 0.23 (0.19) for the  $\Omega = 1$  ( $\Omega_0 = 0.2$ ) sample. The bias and scatter both increase with cluster radius (decreasing  $\delta_c$ ). The bias increases because the true density profiles are steeper than the assumed isothermal value, while the dispersion increases because of the longer dynamical timescales characteristic of larger radii.
- We find a strong correlation between  $r_{\delta_c}$ , the radius encompassing a mean density contrast  $\delta_c$ , and  $T_{\rm X}$ , the broad beam, emission-weighted gas temperature. This scaling a reflection of the similarity between clusters of different mass and their near virial equilibrium state can be used to generate mass estimates with smaller variance than that of the  $\beta$ -model. The degree of scatter is surprisingly small. At  $\delta_c = 1000$ , the standard deviation is 0.11 (0.12) for the  $\Omega = 1$  ( $\Omega_0 = 0.2$ ) sample. The larger dispersion in the  $\beta$ -model method arises because two parameters,  $\beta$  and  $T_{\rm X}$ , contribute independent sources of error whereas the scaling law method incurs error from only one parameter,  $T_{\rm X}$ .

The results from the experiments reported here and those from other experiments cited

above practically rule out the possibility of large systematic errors in the mass determination of galaxy clusters. The large baryon fractions measured in clusters therefore remain difficult to reconcile with standard primordial nucleosynthesis in an  $\Omega = 1$  universe.

This research was supported by NASA through Grants NAGW-2367 and NAG5-2790, by a NATO International Travel Grant and by the NSF through Grant No. PHY94-07194. AEE and JFN are grateful for the hospitality provided by the ITP at UCSB during the "Radiation Backgrounds and Galaxy Formation" workshop and thank D. Bond, C. Norman, J. Ostriker and S. White for their organizational efforts. C.A.M. acknowledges support from a Rackham Predoctoral Fellowship and a Sigma Xi Grant-In-Aid of Research at the University of Michigan, and the Department of Energy and NASA Grant NAG5-2788 at Fermilab.

Label	N	Description	Reference
EJ	14	$\Omega = 1$ , $\sigma_8 = 0.59$ , wind ejection included	Metzler & Evrard (1994,5)
2F	14	same as EJ without winds	"
NFW	6	$\Omega = 1,  \sigma_8 = 0.63,  \text{Tree/SPH code}$	Navarro et al. (1995a)
EdS	8	$\Omega = 1,  \sigma_8 = 0.59,  \text{no feedback}$	Evrard <i>et al.</i> (1993)
Fl2	8	$\Omega_0 = 0.2$ , $\lambda_o = 0.8$ , $\sigma_8 = 1$ , same IC's as EdS	"
Op2	8	$\Omega_0 = 0.2, \ \lambda_o = 0, \ \sigma_8 = 1,$	"

 ${\bf Table~2}$  Synthetic Observation Parameters

_	
Parameter	value
source redshift $z$	0.04
exposure time $t_{exp}$ (sec)	7200
background noise level $S_N^a$	$3 \times 10^{-4}$
background subtraction level $S_b{}^a$	$3 \times 10^{-4}$
minimum surface brightness in fit $S_{min}^{\ a}$	$3 \times 10^{-4}$

 $<sup>^</sup>a$  units : ROSAT cnts s<sup>-1</sup> arcmin<sup>-2</sup>.

$\langle v_r \rangle / c_s$	$\langle v_r^2 \rangle / c_s^2$
$0.001 \pm 0.016$	$0.041 \pm 0.010$
$-0.022 \pm 0.022$	$0.069 \pm 0.018$
$-0.080 \pm 0.119$	$0.261 \pm 0.077$
$-0.008 \pm 0.033$	$0.112 \pm 0.019$
$-0.012 \pm 0.004$	$0.022 \pm 0.009$
$-0.005 \pm 0.014$	$0.045 \pm 0.020$
	$0.001 \pm 0.016$ $-0.022 \pm 0.022$ $-0.080 \pm 0.119$ $-0.008 \pm 0.033$ $-0.012 \pm 0.004$

	$\Omega = 1$		$\Omega_0 = 0.2$	
$\delta_c^{est}$	$ar{\mathcal{X}}^a$	$\sigma_{\mathcal{X}}$	$ar{\mathcal{X}}^a$	$\sigma_{\mathcal{X}}$
100	1.46	0.53	2.08	0.50
250	1.15	0.36	1.60	0.33
500	1.02	0.29	1.34	0.24
1000	0.94	0.23	1.15	0.19
2500	0.87	0.16	1.00	0.14

 $<sup>^{</sup>a}\mathcal{X} = M^{est}/M^{true}$ .

Table 5
Scaling Law Accuracy

	$\Omega = 1$		$\Omega_0 = 0.2$	
$\delta_c$	$r_{10}(\delta_c)^a$	$\sigma_{\mathcal{X}}$	$r_{10}(\delta_c)^a$	$\sigma_{\mathcal{X}}$
100	4.89	0.20	4.78	0.20
250	3.37	0.18	3.31	0.16
500	2.48	0.15	2.48	0.14
1000	1.79	0.11	1.87	0.12
2500	1.11	0.08	1.25	0.10

 $<sup>^</sup>a$  Defined by equation (8), units are Mpc ( $h\!=\!0.5).$ 

### References

Bartelmann, M., 1995, A&A, 299, 11.

Bartelmann, M., Steinmetz, M. & Weiss, A. 1995, A&A, 297, 1.

Bartlett, J.G., Blanchard, A., Silk, J. 1995, Science, 267, 980.

Bertschinger, E. 1985, ApJS58, 39.

Bertschinger, E. 1987, ApJ, 323, L103.

Bird, C.M. 1995, ApJ, 445, L81.

Briel, U.G. & Henry, J.P. 1994, Nature, 372, 439.

Briel, U.G., Henry, J.P., & Böhringer, H. 1992, A&A, 259, L31.

Briel, U.G., Henry, J.P., Schwarz, R.A., Böhringer, H. & Ebeling, H., Edge, A.C., Hartner, G.D., Schindler, S., Trümper, J. & Voges, W. 1991, A&A, 246, L10.

Bonnet, H., Mellier, Y. & Fort, B. 1994, ApJ, 427, L83.

Buote, D.A. & Tsai, J. C. 1995, ApJ, in press.

Carr, B. 1993, Nature, 363, 16.

Cavaliere, A. & Fusco-Femiano, R. 1976, A&A, 49, 137.

Cen, R. & Ostriker, J.P. 1992, ApJ, 399, L113.

Copi, C.J., Schramm, D.N. & Turner, M.S. 1995, Science, 267, 192.

Crone, M.M., Evrard, A.E. & Richstone, D.O. 1994, ApJ, 434, 564.

Crone, M.M., Evrard, A.E. & Richstone, D.O. 1995, ApJ, submitted.

David, L.P., Jones, C. & Forman, W. 1995, ApJ, 445, 578.

Dressler, A. & Shectman, S.A. 1988, AJ, 95, 985.

Durret, F., Gerbal, D., Lachièze-Ray, G., Lima-Neto, G. & Sadat, R. 1994, A&A, 287, 733.

Evrard, A.E. 1990, ApJ, 363, 349.

Evrard, A.E., Mohr, J.J., Fabricant, D.G. & Geller, M.J. 1993, ApJ, 419, L9.

Fahlman, G., Kaiser, N., Squires, G. & Woods, D. 1994, ApJ, 437, 56.

Freedman, W. et al. 1994, Nature, 371, 757.

Gunn, J.E., & Gott, J.R. 1972, ApJ, 209, 1

Hata, N., Scherrer, R.J., Steigman, G., Thomas, D. & Walker, T.P. 1994, OSU-TA-26/94.

Hoffman, Y. 1988, ApJ, 328, 489.

Hughes, J. P. 1989, ApJ, 337, 21.

Ikebe, Y. et al. 1994, in *Clusters of Galaxies*, eds. F. Durret, A. Mazure & J. Tranh Thanh Van, (Gif-sur-Yvette: Editions Frontieres), p. 167.

Krauss, L. & Kernan, P.J. 1994, ApJ, 432, L79.

Loeb, A. & Mao, S. 1994, ApJ, 435, L109.

Miralde-Escudé, J. & Babul, A. 1995, ApJ, 449, 18.

Miyaji, T. et al. 1993, ApJ, 419, 66.

Metzler, C.A. & Evrard, A.E. 1994, ApJ, 437, 564.

Metzler, C.A. & Evrard, A.E. 1995, in preparation.

Mohr, J.J., Evrard, A.E., Fabricant, D.G., & Geller, M.J. 1995, ApJ, 447, 8.

Mould, J. et al. 1995, ApJ, 449, 413.

Mushotzky, R. 1994, in *Clusters of Galaxies*, eds. F. Durret, A. Mazure & J. Tranh Thanh Van, (Gif-sur-Yvette: Editions Frontieres), p. 167.

Navarro, J.F., Frenk, C.S. & White, S.D.M. 1995a, MNRAS, 275, 720.

Navarro, J.F., Frenk, C.S. & White, S.D.M. 1995b, ApJ, submitted.

Navarro, J.F. & White, S.D.M., (1993) MNRAS, 265, 271.

Navarro, J.F. & White, S.D.M., (1994) MNRAS, 267, 401.

Neumann, D.M. & Böhringer, H. 1995, A&A, in press.

Pearce, F., Thomas, P.A. & Couchman, H.M.P. (1994) MNRAS, 268, 953.

Pildis, R.A., Bregman, J.N. & Evrard, A.E. 1995, ApJ, 443, 514.

Ponman, T.J., Allan, D.J., Jones, L.R., Merrifield, M., McHardy, I.M., Lehto, H.J., & Luppino, G.A. 1994, Nature, 369, 462.

Rottgering, H., Snellen, I., Miley, G., DeJong, J.P., Hanisch, R.J. & Perley, R. 1994, ApJ, 436, 654.

Sasselov, D. & Goldwirth, D. 1995, ApJ, 444, 5.

Schindler, S. 1995, A&A, in press.

Schindler, S. & Böhringer, H. 1993, A&A, 269, 83.

Schindler, S. & Müller 1993, A&A, 272, 137.

Smail, I., Ellis, R.S., Fitchett, M.J. & Edge, A.C. 1995, MNRAS, 273, 277.

- Squires, G., Kaiser, N., Babul, A., Fahlman, G., Woods, D., Neummann, D. & Böhringer, H. 1995, preprint (astro-pg/9507008).
- Steigman, G. 1995, in *The Light Element Abundances*, ed. P. Crane (Berlin: Springer), in press.
- Tsai, J.C., Katz, N. & Bertschinger, E. 1994, ApJ, 423, 553.
- Tyson, J.A., Valdes, F. & Wenk, R.A. 1990, ApJ, 349, L1.
- Walker, T.P., Steigman, G., Schramm, D. N., Olive, K. A., & Kang, H. 1991, ApJ, 376, 51.
- Watt, M. P., Ponman, T. J., Bertram, D., Eyles, C. J., Skinner, G. K., & Willmore, A.P. 1992, MNRAS, 258, 738.
- White, D.A. & Fabian, A.C. 1995, MNRAS, 273, 72.
- White, S. D. M., Navarro, J. F., Evrard, A. E., & Frenk, C. S. 1993, Nature, 366, 429.

# **Figure Captions**

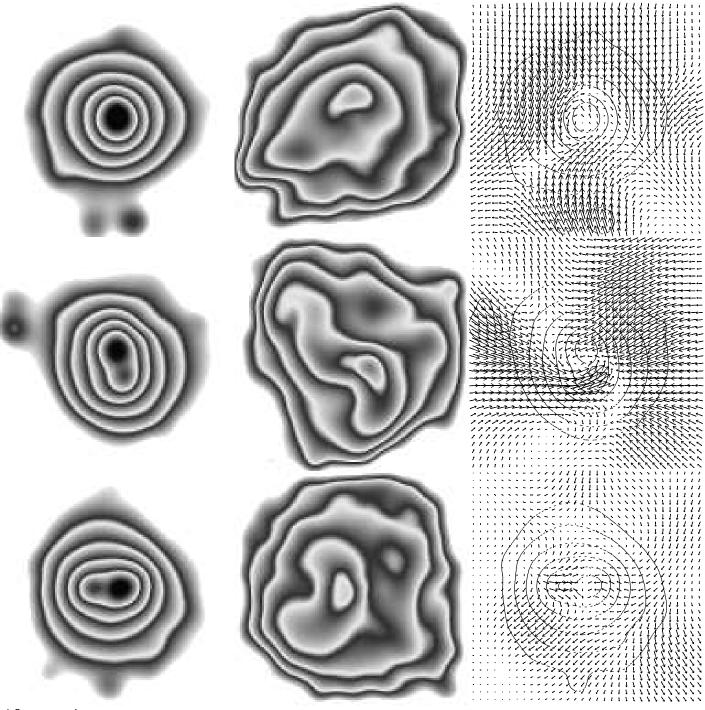
- Figure 1. Synthetic ROSAT X-ray surface brightness (left column), emission weighted temperature (center column) and emission weighted, projected velocity field (right column) for three orthogonal projections of a single cluster from the EdS sample. The cluster is at an assumed redshift z=0.04 and bars in the figure show a 10' angular scale. In the grey scale contours, the dark (or light) bands are logarithmically spaced by factors of  $10^{0.6}$  in surface brightness,  $10^{0.2}$  in temperature, with the third from minimum dark band representing  $10^{-3}$  cnts s<sup>-1</sup> arcmin<sup>-2</sup> and  $10^7$  K, respectively. The velocity vectors are spaced every 2', and scaled such that 1'=1000 km s<sup>-1</sup>.
- **Figure 2.** Projected azimuthally averaged X-ray surface brightness (top) and emission weighted temperature (bottom) for the cluster shown in Figure 1. The top to bottom lines correspond to the top to bottom projections, with data for the middle and bottom projections displaced by factors of 10 (2) and 100 (4) for the surface brightness (temperature) with respect to the top projection.
- Figure 3. Radial Mach numbers  $\langle v_r \rangle/c_s$  (left) and  $\langle v_r^2 \rangle/c_s^2$  (right) derived from the gas sound speed  $c_s^2(r) = 5kT(r)/3\mu m_p$  and the first and second moments of the radial velocity field for all the runs in the ensemble. All quantities are local values measured in radial shells. The overdensity  $\delta_c$  is used as a radial coordinate; note the inverted axis. The dashed line shows  $\delta_c = 500$ , our conservative estimate for the boundary of the hydrostatic region.
- **Figure 4.** Scaling between cluster size, as measured by  $r_{500}$ , and emission weighted temperature for all the models. Symbol types correspond to different models, as shown in the legend. The data are well fit by equation (5). Each model appears three times, from three orthogonal projections.
- **Figure 5.** Three dimensional temperature profiles for all the clusters in the ensemble. The temperature in radial bins is expressed in terms of the average, emission weighted temperature  $T_{\rm X}$  and radius is normalized to the cluster size  $r_{500}$ .
- **Figure 6.** Accuracy of the  $\beta$ -model mass estimates as a function of the estimated density contrast  $\delta_c^{est}$ , equation (6), for the ensemble. Each model appears three times, from orthogonal projections.
- **Figure 7.** Histograms of the estimated-to-true mass ratios derived from the  $\beta$ -model evaluated at three different estimated density contrasts. Dashed vertical lines show an error of  $\pm 40\%$ .
- Figure 8. X–ray surface brightness maps of the six worst underestimates from the  $\Omega=1$  ensemble. Values of the estimated-to-true mass ratio are shown above each panel. Within each panel, the light and bold circles represent the true and estimated values of  $r_{500}$ , respectively. Strongly bimodal or complex images usually result in poor β-model mass

estimates.

Figure 9. Histogram of the estimated-to-true mass ratios from the  $\beta$ -model for the  $\Omega = 1$  combined sample at  $\delta_c^{est} = 500$ .

Figure 10. Histogram of the estimated-to-true mass ratios from the scaling law method for the  $\Omega=1$  combined sample at  $\delta_c=500$ . The distribution is unbiased by construction.

Figure 11. Scatter plot of the deviations in  $\beta$  and  $T_X$  (defined in the text) for all the models in the ensemble. Point styles are the same as those used in Figure 4.



10 arcmin

